Accepted Manuscript

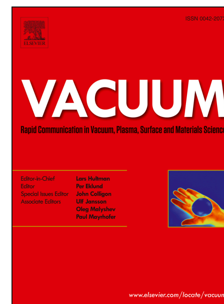

Impact of sublayer thickness and annealing on silicon nanostructures formation in *a*-Si:H/*a*-SiN_x:H superlattices for photovoltaics

Pavel Calta, Pavol Šutta, Rostislav Medlín, Marie Netrvalová

PII: S0042-207X(18)30293-8

DOI: 10.1016/j.vacuum.2018.04.009

Reference: VAC 7914

To appear in: *Vacuum*

Received Date: 26 February 2018

Revised Date: 4 April 2018

Accepted Date: 5 April 2018

Please cite this article as: Calta P, Šutta P, Medlín R, Netrvalová M, Impact of sublayer thickness and annealing on silicon nanostructures formation in *a*-Si:H/*a*-SiN_x:H superlattices for photovoltaics, *Vacuum* (2018), doi: 10.1016/j.vacuum.2018.04.009.

This is a PDF file of an unedited manuscript that has been accepted for publication. As a service to our customers we are providing this early version of the manuscript. The manuscript will undergo copyediting, typesetting, and review of the resulting proof before it is published in its final form. Please note that during the production process errors may be discovered which could affect the content, and all legal disclaimers that apply to the journal pertain.

ACCEPTED MANUSCRIPT

MANUSCRIPT – Vacuum journal

Title: Impact of sublayer thickness and annealing on silicon nanostructures formation in *a*-Si:H/*a*-SiN_x:H superlattices for photovoltaics

Authors: Pavel Calta*, Pavol Šutta, Rostislav Medlín, Marie Netrvalová

Affiliation: University of West Bohemia, New Technologies - Research Centre, Univerzitní 8, 306 14 Plzeň, Czech Republic

*Corresponding author: pcalta@ntc.zcu.cz

Abstract

In this work, we synthesized amorphous multilayered *a*-Si:H/*a*-SiN_x:H superlattices with different thickness of sublayers grown on silicon and quartz substrates by PECVD method at low power density (60 mW/cm^2) and subtrate temperature (250°C) using nitrogen and silane gases as reactive precursors. Subsequently, the post-deposition annealing of these structures, composed of alternating layers of *a*-Si:H and *a*-SiN_x:H, was carried out up to 1100° in vacuum to form silicon nanostructures. The dependence of the structural and chemical bonding characteristics of prepared superlattices on the silicon sublayer thickness and post-deposition annealing temperature was investigated. The formation of silicon nanostructures was confirmed by transmission electron microscopy, X-ray diffraction measurement and Raman scattering spectroscopy. Changes in bonding configuration during the annealing were carried out by Fourier transform infrared spectroscopy. Optical properties were studied by UV-Vis spectroscopy. XRD, Raman and TEM measurements show that the crystallization process of *a*-Si:H sublayers strongly depends on the thickness of initial *a*-Si:H sublayers and the post-deposition treatment process. It was found that a higher crystallization temperature for the thinner *a*-Si:H sublayers is needed. Results clearly show that structural and optical characteristics of these systems can be controlled by deposition parameters and post-deposition annealing conditions.

Keywords: *Superlattice; Silicon nanocrystal; Silicon nitride; PECVD; Transmission electron microscopy; X-ray diffraction*

1 Introduction

Solar energy is the most promising renewable energy source for the replacement of fossil fuels. The need for the sustainable energy sources has led to innovative methods and highly efficient materials to improve the performance and stability of photovoltaic devices. However, the still low efficiency of most used silicon based photovoltaics is mainly due to extremely poor optical properties of bulk silicon and the energy mismatch between the solar spectrum and the silicon bandgap. Crystalline silicon is an indirect bandgap semiconductor, with bandgap energy of 1.12 eV at room temperature. Its absorption of solar spectrum is very poor as the associated energies of most photons coming from sun lay much above the silicon energy gap. The energy excess of those photons with respect to the bandgap energy is released into the matrix via transfer to phonons in a thermalization process. According to the calculated Shockley–Queisser limit, the maximum achievable conversion efficiency of a single p-n junction cell is limited to 33.7% [1].

Many approaches have been adopted for overcoming this efficiency limit [2]. An increase of the conversion can be achieved by the use of multiple energy threshold devices (e.g. tandem solar cells) containing size-controlled silicon nanocrystals (Si-NCs) as an absorber. When the diameter of the Si-NCs is smaller than the Bohr radius (~ 5.29 nm), the quantum confinement effect starts to contribute to the extraction and generation of the excitons [3-5]. This very active field of research has been since the 1990s with the observation of strong light emission in the visible range from porous silicon at room temperature [6, 7]. In nano-scaled superlattice structures, Si sublayers and Si dielectric sublayers (Si_3N_4 [8,9] or SiO_2 [10-12]) are alternately deposited in a stack and subsequently treated with a post-deposition high temperature (~ 1100 °C) annealing. Silicon sublayer thickness should not exceed the critical value predicted by the quantum confinement model. In addition, the thickness of the Si sublayer can be adjusted very accurately and a controllable size and distribution of silicon nanocrystals can be obtained by changing of deposition conditions and parameters [8, 10, 11, 13, 14]. Recently, different approaches have been used to fabricate Si-NCs, such as molecular beam epitaxy (MBE) [7], magnetron sputtering [3], co-sputtering [15], thermal oxidation [3], plasma-enhanced chemical vapor deposition [10,11]. Plasma-enhanced chemical vapour deposition (PECVD) is a powerful method to prepare superlattices required for the fabrication of optoelectronic device and solar cells [16].

However, the influence of the thickness of a-Si sublayer as well as the post-deposition treatment method on crystallization processes and the mechanism responsible for observed room temperature PL from Si-NCs are still unclear. In order to distinguish the mechanisms of luminescence in silicon superlattices, firstly, it is important to prepare well-controlled Si nanostructures and to investigate their structural and optical properties, which are desirable for understanding of the mechanisms in superlattices. In most previous studies, optical and structural properties from Si/SiO_2 multilayers have been investigated [4,10,11,13, 17]. Nevertheless, the high band offsets of the SiO_2 matrix with nanocrystalline silicon nanocrystals can suppress the tunneling probability of carriers into the NCs in devices designed for electroluminescent and photovoltaic applications. In contrast, there is an interest in developing such Si-NCs in a lower bandgap matrix such as Si_3N_4 as it offers smaller band offsets, which in turn can enhance the electrical carrier injection for more efficient silicon-based devices [18]. The research idea on constrained crystallization in a-Si:H/SiN_x:H multilayered films for fabrication of Si-NCs was first published in ref [19]. Wang et al. [8] studied the influence of silicon sublayer thickness and used different post-treatments for iniciation of crystallization, which is generally known important step for Si-NCs formation. The theoretical model for constrained crystallization of silicon based multilayers was published in ref [20]. Silicon nitride based layers are often grown using silane (SiH_4) and ammonia (NH_3) as silicon and nitrogen precursors, respectively and their content can be easily tuned by changing their fractions in the gas mixture [21]. Nevertheless, there is practically no publication that studies silicon based superlattices with NH_3-free silicon nitride barrier sublayers grown from silane and nitrogen.

This paper describes the fabrication and investigation of silicon nanostructures formed in annealed *a*-Si:H/*a*-SiN_x:H multilayers with total thickness of about 500 nm and various sublayer thickness deposited by rf (13.56 MHz) PECVD technique in a single deposition chamber at 250°C on various substrates using SiH_4 and N_2 as precursor gases. Subsequently, the post-deposition annealing of these structures, composed of up to 121 alternate sublayers of *a*-Si:H and *a*-SiN_x:H, was carried out up to 1100°C in vacuum to form Si-nanostructures. The very detailed structural and optical characterization of as-deposited and annealed superlattices is presented, using widely developed techniques such as X-ray diffraction, transmission electron microscopy, Raman scattering, Fourier transform infrared and UV-Vis spectroscopies. The dependence of the microstructural and chemical bonding characteristics of superlattices on the silicon sublayer thickness and post-deposition annealing temperature was

ACCEPTED MANUSCRIPT

investigated. The results revealed that the crystallization process of a-Si:H sublayers strongly depends on both the thickness of the initial a-Si:H sublayers and the post-deposition treatment process. We found that by varying the sublayer thickness in superlattices and post-deposition annealing, it is possible to change the microstructural and optical properties of the superlattice structures.

2 Experimental details

2.1 Material fabrication

In this work, a series of amorphous hydrogenated multilayered *a*-Si:H/*a*-SiN_x:H superlattices were deposited by a capacitively-coupled radiofrequency (13.56 MHz) plasma-enhanced chemical vapor (PECVD) SAMCO 220N deposition system using SiH_4 (10% diluted in Ar) and N_2 as precursor gases. The PECVD system has a parallel planar discharge system, which uses a circular rf electrode (upper) and a substrate electrode (lower). The chamber was pre-evacuated to a base pressure of 10^{-5} Pa by using a combination of roots and turbomolecular pumps. All samples of total thickness of around 500 nm were prepared on (100)-oriented Si wafer and quartz plates. Superlattice samples were composed of alternating amorphous uniformly thick (5, 10, 15 or 20 nm) sublayers of *a*-SiN_x:H and *a*-Si:H followed by a final *a*-SiN_x:H capping sublayer of the same thickness. The multilayered samples with up to 121 sublayers (details in Table 1) were prepared by layer-by-layer deposition with a plasma interuption. Each thin *a*-SiN_x:H barrier sublayer was grown using decomposition of N_2 and SiH_4 precursor gas mixture ($R = N_2/SiH_4 = 120$), while the *a*-Si:H sublayer was grown by pure SiH_4 (10% in Ar). The thickness of each individual sublayer was controlled by adjusting the deposition time. The other deposition conditions are detailed in Table 2.

The common procedure to convert the amorphous silicon phase in the films into nanocrystals (NCs) is using high temperature annealing (Fig. 1). Subsequently after sample deposition, the as-deposited multilayered films were heat-treated to 1100°C in vacuum for 30 minutes at final temperature (600, 700, 800, 1000 and 1100°C) to induce Si nanocrystals formation. For samples discussed in this work, the furnace annealing was performed starting with slow (15 °C/min) ramping temperature from room to the final temperature. To minimize the thermal stress, the temperature was then slowly reduced to 200 °C before the samples were removed from the furnace.

ACCEPTED MANUSCRIPT

ACCEPTED MANUSCRIPT

2.2 Material characterization

The thickness of films was determined by KLA-Tencor P-6 Surface Profiler and compared to the calculated values from UV-Vis spectra (Table 1). The chemical composition of the silicon nitride layer was analyzed by energy dispersive X-ray spectroscopy (EDS) as a part of scaning electron microscope Jeol JSM 7600F (100 V-30 kV, 25-1000000x, resolution of 1 nm at 15kV). Transmission electron microscopy (TEM) investigations were performed on Jeol JEM 2200FS (80-200kV, in-column omega filtr, TEM mode from 50 to 1500 000x, STEM mode from 100x to 150 000 000x). The microstructure of as-deposited and annealed films was studied by X-ray diffraction analysis (XRD) using an automatic powder diffractometer X'Pert Pro with the thin film configurations (fixed and small incident angle, asymmetric geometry) and ultra-fast semiconductor detector Pixcel and CuKα characteristic radiation (λ = 0.154 nm). The chemical bonding configuration was investigated by Fourier-transform infrared spectroscopy (FTIR) performed on spectrometer Nicolet 380 from 650 to 4000 cm^{-1} and at an instrumental resolution of 4 cm^{-1} by using Attenuated total reflectance (ATR) accesory with germanium crystal. Raman spectra of samples were recorded at room temperature with Raman DXR microscopy with an excitation by the 532 nm laser (1 mW) in back-scattering geometry. The optical properties (transmittance, optical band-gap) of the samples were investigated by UV-VIS spectrophotometer Specord 210 working in the range of 190–1100 nm.

3 Results and discussion

By changing the gas flow ratio (R = N_2/SiH_4) and plasma interruption, four sets of samples with multilayered structure were obtained by up to 121 alternate single sublayers of *a*-Si:H (R = 0, deposition rate of 32.1 nm/min, E_g = 1.75 eV) and *a*-SiN_x:H (R = 120, deposition rate of 10.9 nm/min, E_g = 3.72 eV, nitrogen content ~ 69.7 %) with the various thickness of 5, 10, 15 or 20 nm. The *a*-SiN_x:H sublayer was deposited as the first and the last to provide good quality interface between silicon substrate and superlattice and to enclose the surface of the silicon core sublayers during high-temperature annealing. After deposition, thermal annealing up to 1100°C in vacuum for 30 min at final temperature was carried out to form silicon nanostructures. To investigate the effect of sublayer thickness and thermal annealing

on the superlattices, their microstructural and optical properties were characterized using XRD, TEM, Raman, FTIR and UV-Vis spectroscopies.

3.1 X-ray diffraction analysis

Fig. 2 shows the XRD patterns of all as-deposited and annealed *a*-Si:H/*a*-SiN_x:H superlattices with various sublayer thickness annealed up to 1100°C in vacuum for 30 minutes at final temperature.

XRD patterns of samples were collected before and after annealing with a constant step of 0.02 deg from 15 to 65 deg of 2ϑ scales, where the three strongest silicon lines are located. In order to find out the real structure of the films (phase analysis, micro-strain and crystallite size evaluation), a line profile analysis was used. The procedure, proposed by Langford [22] based on a Voigt function analyzing the breadths of diffraction lines (FWHM and integral breadth β = area/I_o, where I_0 is the intensity at the line profile maximum) was used. Alumina powder from NIST was used as an instrumental standard. A single line procedure was used [23]. In general, the line broadening is caused mainly by two effects: (i) finite dimensions of coherently diffracting domains (size) and (ii) micro-strains. The measured diffraction line profile of the analysed specimen can be described as an outcome of convolution of the structurally broadened only profile, which is desired and the instrumentally broadened profile. The other de-convolution, which has to be taken into account, is separating of Cauchy and Gaussian components of the integral breadths. Finally, the average size $\langle D \rangle$ and strains $\langle \varepsilon \rangle$ are obtained using the Cauchy and Gaussian integral breadth components of the structural profile using the following formulae:

$$\langle D \rangle = \lambda / \beta_C^{f}.\cos\vartheta \quad (1)$$

$$\langle \varepsilon \rangle = \beta_G^{f} / 4\tan\vartheta \quad (2)$$

where λ is the characteristic wavelength used and ϑ is the Bragg angle of the investigated line. Table 3 shows the variation of calculated crystallite sizes and microstrains of the annealed samples by using Eq. (1) and (2), respectively.

In XRD patterns of as-deposited films, there are broad diffraction lines, which represent amorphous state of material. At temperature of 600°C, nearly the same broad diffraction lines are detected. It can be attributed to the persistent amorphous state or to very small Si nanoclusters which are not visible in XRD analysis. While the annealing temperature increased to 700 °C, first sharp diffraction lines were observed (ML20 and ML15 samples). Annealed samples show three diffraction lines at 28.5°,

47.7°, and 56.3° corresponding to (111), (220), and (311) lines of cubic Si phase, respectively and the intensity of the lines further increases. As shown in Fig. 2, the diffraction line intensities of crystalline Si increase with the increasing annealing temperature. The higher annealing temperature catalyzes the creation of new Si-NCs as well as the size of already existed Si-NCs. This is then followed by a coalescence phenomenon due to the continuous growth of NCs in the superlattice. The increase in line intensities, as a function of annealing temperature and silicon sublayer thickness, indicates a higher volume of phase transformation from the amorphous to crystalline Si. The Si-NC size is found to be limited by the thickness of the silicon sublayer.

Crystallites obtained from XRD is in this case only very rough and can vary from sample to sample according to the initial interfacial conditions during the film deposition. It is only important that they are in the nano-meter scale (about or less than 10 nm in average). In case of samples with the silicon sub-layers of 15 and 20 nm thick bi-modal crystallite sizes were observed and it correspond to the results described in ref [8, 20]. An interesting phenomenon arose in the annealing stage: higher crystallization temperature is needed for superlattices having thinner layers, because a very thin layer has large surface to volume ratio and needs more energy to reach the phase transformation. An theoretical model, according to experiment data from silicon nitride based multilayers, has been developed and described in [20]. Using this approach, we can conclude that the crystallization process has similar behaviour during post-deposition treatment.

3.2 Transmission electron microscopy

Silicon nanostructures embedded in the silicon sublayers were confirmed by transmission electron microscopy. It is a powerful tool for making images of the nanoscale structures [24, 25]. The low resolution bright field of the selected as-deposited and annealed a-Si:H/a-SiN_x:H superlattice with the initial sublayer thickness of 15 nm (ML15 sample) are shown in Fig. 3 (a) and (b), respectively. Defocused images were captured to show the overall sublayers in multilayered structure.

The degree of crystallinity of as-deposited and annealed sample can be qualitatively estimated by the selected area electron diffraction (SAED) patterns as shown in left insets in Fig. 3 (a) and (b), respectively. SAED patterns shown in the left inset in Fig. 3 (a) reveals that as-deposited ML15 sample is essentially amorphous as other prepared as-deposited samples (not presented). The left inset in Fig. 3 (b)

with electron diffraction pattern of ML15 sample annealed to 1000°C in vacuum represents three sharp intense bright rings which correspond to the <111>, <220> and <311> lattice planes of crystalline cubic silicon [26].

High-resolution TEM (HRTEM) images of the as-deposited and annealed samples are shown in the right insets in Fig. 3(a) and (b), respectively. The right inset in Fig. 3(a) shows high resolution TEM image of the as-deposited ML15 superlattice and its amorphous structure. These HRTEM image shows many clear lattice fringes of sublayers and the alternating light and dark patterns are clearly visible and correspond to the silicon and silicon nitride layers in multilayered sample, respectively. Dotted white lines have been superimposed on the images as a guide to the eye. Also, these distinct regions have approximate thickness of ~ 15 nm. The right inset in Fig. 3 (b) gives the high resolution TEM image of the annealed ML15 sample and reveals the crystallization in Si sublayers. The dark and bright segments arise due to the density difference between the crystalline and amorphous regions, respectively [27]. It is clearly shown that the Si nanocrystals with high density can be well identified and were formed in the initial a-Si:H layers after annealing up to 1000°C in vacuum. Most of the Si-NCs are sitting uniformly in the a-Si layer with different orientations. The results of this analysis show that the diameters of Si-NCs vary in the range from 3 to 9 nm and it corresponds with the XRD results. The size of formed Si-NCs are limited by the initial sublayer thickness and therefore can be well confined. The TEM results also demonstrated that the as-deposited amorphous SiN_x sublayers still keep their amorphous structure after post-deposition annealing.

Nevertheless, the experimental results obtained from the X-ray diffraction (XRD) analysis and transmission electron microscopy (TEM) cannot be compared in general, but they can support each other. It is necessary to know that the XRD is a “global method” giving information from large volume, on the other hand, TEM is a “local method” giving information from a very small volume. But the results from the X-ray diffraction and electron diffraction can be compared. It means that the crystallite dimensions obtained from XRD analysis is an average value from a lot of crystallites in the volume probed. It is important to observe that the HRTEM images show the co-existence of amorphous and crystalline silicon which indicates that the nc-Si:H sub-layer does not only contain the crystalline part, it also includes the amorphous silicon as well and the amount of crystallinity does depend on the thickness of that sublayer. Moreover, the quality of superlattice samples undergoes no obvious changes during annealing. This

ACCEPTED MANUSCRIPT

means that furnace annealing technique with slowly increasing temperature during post-deposition annealing can avoid damage to the multilayered structures.

3.3 Raman scattering spectroscopy

Raman scattering is a useful complementary tool, nondestructive, and capable of determining the information about the crystalline and amorphous phases of material. The crystalline nature of the superlattices and the formation of the Si nanostructures has been investigated using Raman spectroscopy in backscattering geometry [28].

Fig. 4(a) shows the first order of Raman spectra collected from all prepared samples with various sublayer thickness as-deposited and annealed up to 1100°C in vacuum for 30 minutes deposited on quartz to eliminate crystalline Si peaks from the substrate. It could be concluded that the state of silicon sublayers in the as-deposited superlattices were amorphous because of the asymetric broad band at ~ 480 cm^{-1} which corresponds to the transverse optical (TO) vibration mode of a-Si:H phase [29,30]. All multilayers showed practically the similar evolution of structure development during annealing. Up to 600°C, the spectral lines of all samples still correspond to the amorphous dominated network. Generally, for amorphous state (Si-NCs smaller than 2 nm), the Raman absorption band is very broad and centered at ~480 cm^{-1} [26, 29, 30]. For multilayers annealed to the temperature of 700°C and higher, the peak intensity of TO vibration mode of a-Si at 480 cm^{-1} diminishes with the increase of annealing temperature and the TO mode of nanocrystalline Si appears as the additional sharp peak at around 514 cm^{-1} [31]. It indicates the formation of nano-crystalline silicon (Si-NCs size > 2 nm) in original amorphous Si sublayers [26]. At 1100°C, amorphous Si has been transformed into crystalline Si, although an amorphous Si shoulder is still detected. Post-deposition annealing temperature for Si-NCs formation is also a function of the a-Si layer thickness in a-Si/SiN_x superlattice. In our study, the crystallization of Si-NCs is observed at lower temperature of 700 °C (ML20 sample) because of the relatively high thickness of 20 nm of a-Si sublayers. In the case of ML5 sample, 5 nm thin a-Si sublayers require relatively higher starting crystallization temperature (over 800°C) to form Si-NCs. This could be due to a more distorted arrangement of atoms near the interface of a-Si and SiN_x layers. Similar results were reported in [8, 17, 32].

ACCEPTED MANUSCRIPT

ACCEPTED MANUSCRIPT

A quantitative estimation of the degree of crystallinity has been done by the deconvolution of each Raman spectrum in the range of 300 – 600 cm^{-1}. Fig. 4(b) shows a representative deconvoluted Raman spectrum of the ML15 sample annealed at 1000°C which shows peaks present in the ranges: the longitudinal acoustic mode LA (250 – 350 cm^{-1}), the longitudinal optical branch mode LO (390 – 450 cm^{-1}) and the transverse optical mode TO (480–550 cm^{-1}), respectively. The TO mode can be deconvoluted into three fitting peaks, namely the a-Si TO (~480 cm^{-1}), the grain boundary TO (~505 cm^{-1}) and the c-Si TO (~520 cm^{-1}) [32-35]. The calculated dimension of the Si nanocrystal with a Raman peak position of 515 cm^{-1} lies in the range 3–5 nm [36-38].

Fig. 4(c) shows the change of the crystalline volume fraction after sample annealing at various temperatures. The crystalline volume fraction of Si thin sublayers was estimated from the relation published elsewhere [37, 38]. The obtained values display that crystalline volume fraction have increased from 0 to 38% for ML5 sample and up to 70% for ML20 sample after post-deposition annealing to 1100°C. Overall, the results are consistent with the XRD and TEM investigations.

3.4 Fourier-transform infrared spectroscopy

Investigation of chemical bonding configuration in the superlattices has been carried out by Fourier-transform infrared spectroscopy (FTIR). FTIR results are shown in Fig 4(a)-(c). FTIR spectra of as-deposited multilayers show Si-N stretching (~ 830 cm^{-1}), Si-H stretching (2000 - 2300 cm^{-1}), N-H stretching (~ 3300 cm^{-1}) and N-H bending (~ 1185 cm^{-1}) modes which are typical for *a*-Si:H and *a*-SiN_x:H layers [39-42].

Several main absorption bands due to Si and H related vibration modes, their peak positions and integrated absorption areas (stretching mode fractions) for all samples have been found and are presented in Fig. 5(a) and Fig. 5(b), respectively. FTIR spectra in the range of 1700-2400 cm^{-1} were measured on superlattices grown on quartz. The main bands in this wavenumber range have been deconvoluted into four Gaussian peaks: H-Si-Si_3 around 2000 cm^{-1} and H-Si-Si_2H around 2090 cm^{-1} correspond to the bands from *a*-Si:H sublayers; H-Si-SiN_2 and H-Si-SiNH around 2170 cm^{-1}, and H-Si-N_3 around 2250 cm^{-1} correspond to the bands from *a*-SiN_x:H sublayers [43]. It can be seen, that while the contribution from *a*-SiN_x:H sublayers is independent on total number of sublayers, the ratio of absorption bands from *a*-Si:H sublayers is changed with different number of sublayers in superlattice.

ACCEPTED MANUSCRIPT

Fig. 5(c) shows the comparison of FTIR spectra of ML15 sample as-deposited and annealed to 1100 °C in the region where the Si-N stretching absorption modes are strongest. In the inset, Si-H and N-H absorption bands become weaker with increasing the annealing temperature and disappear after annealing at 600°C, which is due to the effusion of hydrogen under thermal treatments.

3.5 UV-Vis spectroscopy

The optical properties of multilayers were studied by UV-Vis absorption spectroscopy. The typical transmittance plots shown in Fig. 6(a) were performed on the multilayers deposited on quartz. Due to the thickness dependent optical interference, the curve of transmittance appears as a periodic fluctuation. Good transparency of all samples was observed. The wavelength dependent transmittance of all superlattices strongly depends on the annealing temperature, as shown in Fig. 6(a). Quantum size effect in the films can be clearly demonstrated when compared the crystallite sizes in Table 1 and “blue shift” in Fig 6(a) (shift of the spectral absorption edge to the shorter wavelengths).

The optical band gap depicted in Fig. 6(b) was determined from the transmittance spectra by using well-known Tauc procedure [44]. Fig. 6(c) illustrates the dependence of the total thickness of superlattice samples calculated from the measured transmittance spectra by method described in [45] and is consistent with TEM measurement.

It can be observed that the band gap and total thickness of superlattices are influenced by the temperature annealing and the drop was most probably a result of mass densification caused by the observed loss of hydrogen and structural changes.

4 Conclusions

To summarize, we have successfully prepared and characterized the structural and optical properties of silicon nanostructures formed by post-deposition thermal annealing of 500 nm thick amorphous *a*-Si:H/*a*-SiN_x:H superlattices prepared by PECVD using silane and nitrogen as precursors. Multilayers composed of up to 121 alternating uniformly thick (20, 15, 10 and 5 nm) sublayers *a*-Si:H and *a*-SiN_x:H were prepared on Si and quartz substrates. The evolution of the microstructural and optical properties of the as-deposited and annealed samples were investigated in detail by using many techniques, such as XRD, TEM, Raman, FT-IR and UV-VIS spectroscopies. The films showed a very good thickness and structure

homogeneity. The amorphous structure of the as-deposited and annealed multilayers to 600°C was revealed from XRD, TEM and Raman measurements. FTIR spectroscopy showed presence of Si-N, Si-H and N-H bonds. Post-deposition treatment to 600°C revealed, that the Si-H and N-H bonds disappeared, which indicated the hydrogen effusion. Annealing treatments at 600°C led to a fall in optical band gap probably as a consequence of hydrogen effusion, while for the higher annealing temperatures, the value of optical band gap increased. The total sample thickness decreased during the annealing. This was most probably as a result of mass densification caused by the observed loss of hydrogen. With next increasing of annealing temperature, XRD, TEM, Raman measurements showed the growth of Si-NCs which originated from the crystallization of the amorphous regions in the initial *a*-Si:H sublayers. XRD study revealed that the crystallites in average are smaller in size with lowering the sublayers thickness. The crystalline mass fraction exceeded 70% for ML20. The amorphous SiN_x sublayers could act as stable barrier and constrain the growth of Si-NCs. The optical absorption contribution of Si-NCs has been revealed. Size of the quantum effect depends mainly on the following factors: (1) sublayer thickness, (2) crystallite sizes, (3) crystalline phase volume content, (4) internal inhomogeneity of the film and on their combinations. To sum up, the results proposed in the present work could have strong implications for the good control of such nanomaterials involved in photovoltaic applications.

Acknowledgements

The result was developed within the CENTEM project, reg. no. CZ.1.05/2.1.00/03.0088, cofunded by the ERDF as part of the Ministry of Education, Youth and Sports OP RDI programme and, in the follow-up sustainability stage, supported through CENTEM PLUS (LO1402) by financial means from the Ministry of Education, Youth and Sports under the "National Sustainability Programme I." The result was developed within CEDAMNF the project, reg. no. CZ.02.1.01/0.0/0.0/15_003/0000358, co-funded by the ERDF as part of the MŠMT. Authors want to thank to Jarmila Savková for the elemental composition of silicon nitride sublayers.

ACCEPTED MANUSCRIPT

ACCEPTED MANUSCRIPT

References

[1] W. Shockley, H. J. Queisser, J. Appl. Phys. 32 (1961) 510–519.

[2] M. A. Green, Third Generation Photovoltaics: Ultra-High Efficiency at Low Cost, Springer-Verlag, 2003.

[3] G. Conibeer, M. Green, R. Corkish, Y. Cho, E.-C. Cho, C.-W. Jiang, T. Fangsuwannarak, E. Pink, Y. Huang, T. Puzzer, T. Trupke, B. Richards, A. Shalav, and K.-L. Lin, Thin Solid Films 511 (2006) 654.

[4] F. Gourbilleau, C. Dufour, B. Rezgui, and G. Bremond, Mater. Sci. Eng. B 159 (2009) 70.

[5] S. Gardelis, A. G. Nassiopoulou, P. Manousiadis, S. Milita, A. Gkanatsiou, N. Frangis, Ch. B. Lioutas, J. Appl. Phys. 111 (2012) 083536.

[6] L. T. Canham, Appl. Phys. Lett. 57 (1990) 1046.

[7] D. J. Lockwood, Z. H. Lu, and J. M. Baribeau, Phys. Rev. Lett. 76 (1996) 539.

[8] L. Wang, X. Wang, X. Huang, Z. Ma, Y. Bao, J. Shi, W. Li, J. Xu, K. Chen, J. Non-Cryst. Solids 299-302 (2002) 751-755

[9] G. Scardera, T. Puzzer, I. Perez-Wurfl, G. Conibeer, J. Cryst. Growth 310 (2008) 3680-3684.

[10] S. Agbo, P. Calta, P. Šutta, V. Vavruňková, M. Netrvalová, L. Prušáková, Phys. Status Solidi A 211, No. 7 (2014) 1512-1518.

[11] S. Agbo, P. Šutta, P. Calta, R. Biswas, B. Pan, Can. J. Phys. 92 (2014) 783-788.

[12] Y. Xu, S. Li, Z. Zhao, Z. Ren, W. Yu, Vacuum 120 (2015) 37-41.

[13] M. Zacharias, J. Heitmann, R. Scholz, U. Kahler, M. Schmidt, J. Bläsing, Appl. Phys. Lett. 80 (2002) 661–663.

[14] A. M. Hartel, D. Hiller, S. Gutsch, P. Löper, S. Estradé, F. Peiró, B. Garrido, M. Zacharias, Thin Solid Films 520 (2011) 121–125.

[15] E.-C. Cho, S. Park, X. Hao, D. Song, G. Conibeer, S.-C. Park, M. A. Green, Nanotechnology 19 (2008) 245201.

[16] A. Shah, P. Torres, R. Tscharner, N. Wyrsch, H. Keppner, Science 285 (1999) 692.

[17] M. Zacharias, J. Blasing, K. Hirschman, L. Tsybeskov, P. M. Fauchet, J. Non-Cryst. Solids (2000) 266–269.

[18] G. Y. Sung, N. M. Park, J. H. Shin, K. H. Kim, T. Y. Kim, K. S. Cho, C. Huh, IEEE J. Sel. Top. Quantum Electron. 86 (2006) 1545–1555.

ACCEPTED MANUSCRIPT

[19] K. Chen,X. Huang,J. Xu,D. Feng, Appl. Phys. Lett. 61 (1992) 2069.

[20] L. Zhang, K. Chen, L. Wang, W. Li, J. Xu, X. Huang, K. Chen, J. Phys.: Condens. Matter. 14 (2002) 10083-10091.

[21] F. Giorgis, C. Vinegoni, L. Pavesi, Phys. Rev. B 61 (2000) 4693–4698.

[22] J. I. Langford, J. Appl. Phys. 11 (1978) 10-14.

[23] R. Delhez, T. H. de Keijser, E. J. Mittemeijer, Fresenius Z. Anal. Chem. 312 (1982) 1-16.

[24] F. Iacona, C. Bongiorno, C. Spinella, S. Boninelli, F. Priolo, J. Appl. Phys. 95 (2004) 3723.

[25] F. Gourbilleau, X. Portier, C. Ternon, P. Voivenel, R. Madelon, R. Rizk, Appl. Phys. Lett. 78 (2001) 3058.

[26] D. Kar, D. Das, J. Mat. Chem. A 1 (2013) 14744-14753.

[27] D. Das, D. Kar, RSC Adv. 6 (2016) 3860-3869.

[28] A. Pérez-Rodríguez, A. Cornet, J. R. Morante, Microelectron. Engrg. 40 (1998) 223–237.

[29] H. Rinnert, M. Vergnat, A. Burneau, J. Appl. Phys. 89 (2001) 237.

[30] H. L. Hao, L. K. Wu, W. Z. Shen, H. F. W. Dekkers, Appl. Phys. Lett. 91 (2007) 201922.

[31] E. Bustarret, M. A. Hachicha, M. Brunel, Appl. Phys. Lett. 52 (1988) 1675.

[32] L.Wang, X. Wang, X. Huang, Z. Li, Z. Ma, L. Zhang, Y. Bao, J. Shi, W. Li, X. Huang, J. Xu, K. Chen, J.Phys. Condens. Matter 13 (2001) 9857–9865.

[33] M. Marinov, N. Zotov, Phys. Rev. B 55 (1997) 2938–2944.

[34] W. Wei, G. Xu, J. Wang, T. Wang, Vacuum 81 (2007) 656–662.

[35] A. M. Funde, N. A. Bakr, D. K. Kamble, R. R. Hawaldar, D. P. Amalnerkar, S. R. Jadkar, Sol. Energy Mater. Sol. Cells 92 (2008) 1217-1223.

[36] G. Faraci, S. Gibilisco, P. Russo, A. R. Pennisi, Phys. Rev. B 73 (2006) 03307.

[37] Y. He, C. Yin, G. Cheng, L. Wang, X. Liu, G.Y. Hu, J. Appl. Phys. 75 (1994) 797.

[38] A. Gajovic, D. Gracin, K. Juraic, J.S. Parramon, M. Ceh, Thin Solid Films 517 (2009) 5453-5458.

[39] G. Scardera, T. Puzzer, G. Conibeer, M.A. Green, J. Appl. Phys. 104 (2008) 104310.

[40] J. Zhao, M. A. Green, IEEE Trans. Electron Devices 8 (1991) 1925–1934.

[41] R. Vernhes, O. Zabeida, J. E. Klemberg-Sapieha, L. Martinu, J. Appl. Phys. 100 (2006) 063308.

[42] X. Xu, D. Zhou, Q. He, Y. Jiang, T. Fan, L. Huang, T. Ao, S. He, Appl. Phys. A Mater. Sci. Process. 111 (2013) 867–876.

[43] A. D. Mallorquí, E. Alarcón-Lladó, I. C. Mundet, A. Kiani, B. Demaurex, Nano Res. 2 (2015) 673.

[44] J. Tauc, Materials Research Bulletin, 3 (1968) 37-46.

[45] J. Očenášek, M. Netrvalová, P. Šutta, APCOM Proceedings (2011) 110-113

ACCEPTED MANUSCRIPT

Figure Captions (figures in color in online version only)

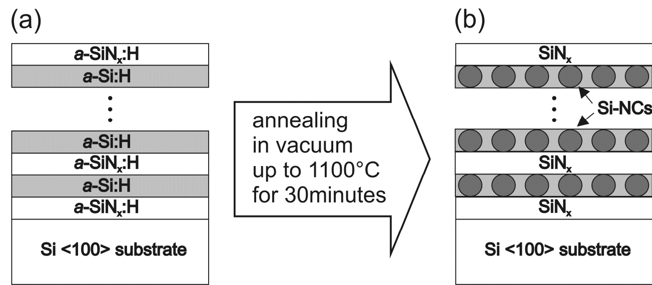

Fig. 1 Schematic illustration of a-Si:H/a-SiN$_x$:H multilayered samples grown on the c-Si substrate before (a) and after annealing (b); Si-nanostructures are formed in a-Si sublayers after annealing.

ACCEPTED MANUSCRIPT

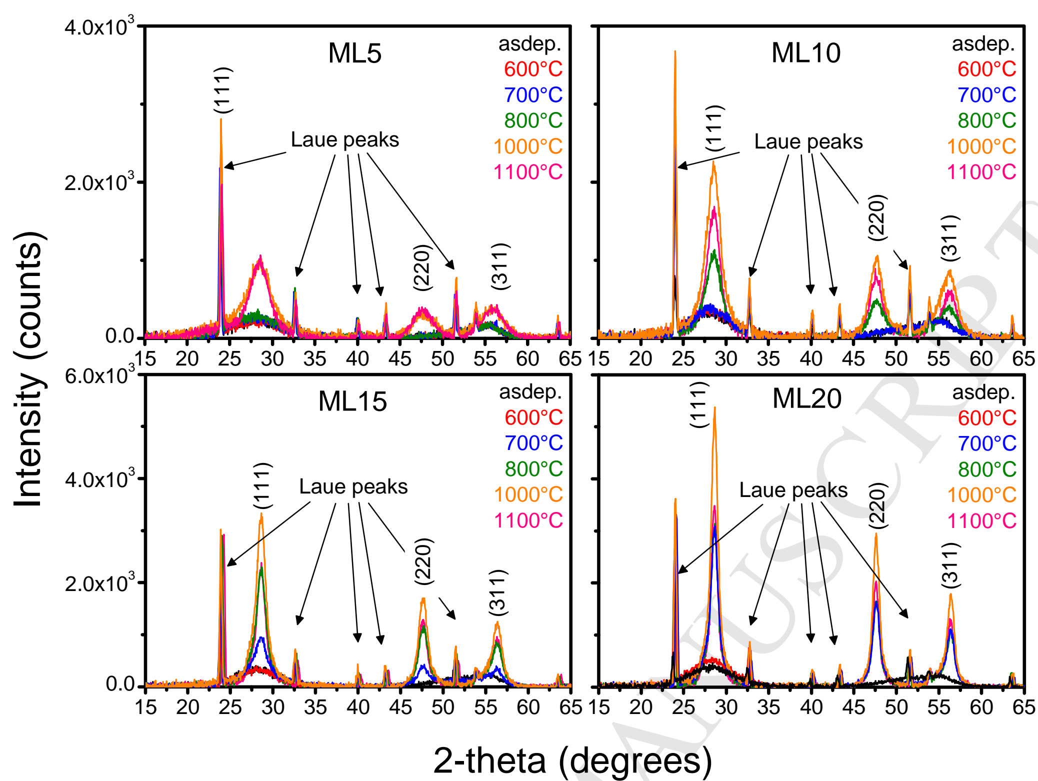

Fig. 2 (a) X-Ray diffraction patterns of the as-deposited and annealed multilayers a-Si:H/a-SiN$_x$:H to 1100°C in vacuum.

ACCEPTED MANUSCRIPT

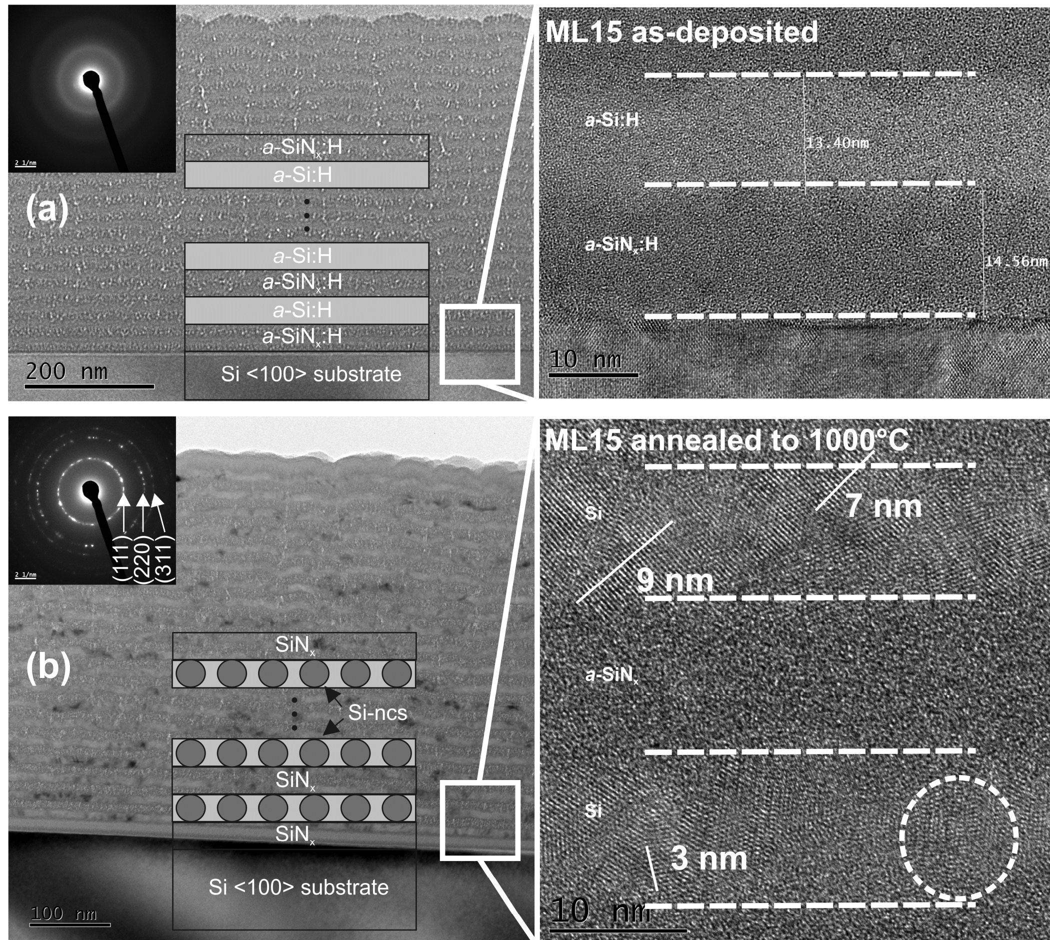

Fig. 3 Cross-section TEM images of as-deposited a-Si:H/a-SiN$_x$:H multilayer with 15 nm thick sublayers (ML15 sample) (a) and annealed to 1000°C in vacuum for 30 minutes (b) obtained on c-Si substrate. The left insets represent the selected area electron diffraction patterns. The right insets show high-resolution TEM images of the superlattices which show amorphous structure (a) and the formation of silicon nanocrystals with sharp boundary with the amorphous silicon (b). Dashed lines serve as guides to the eye to clearly show the interface between silicon and silicon nitride sublayers.

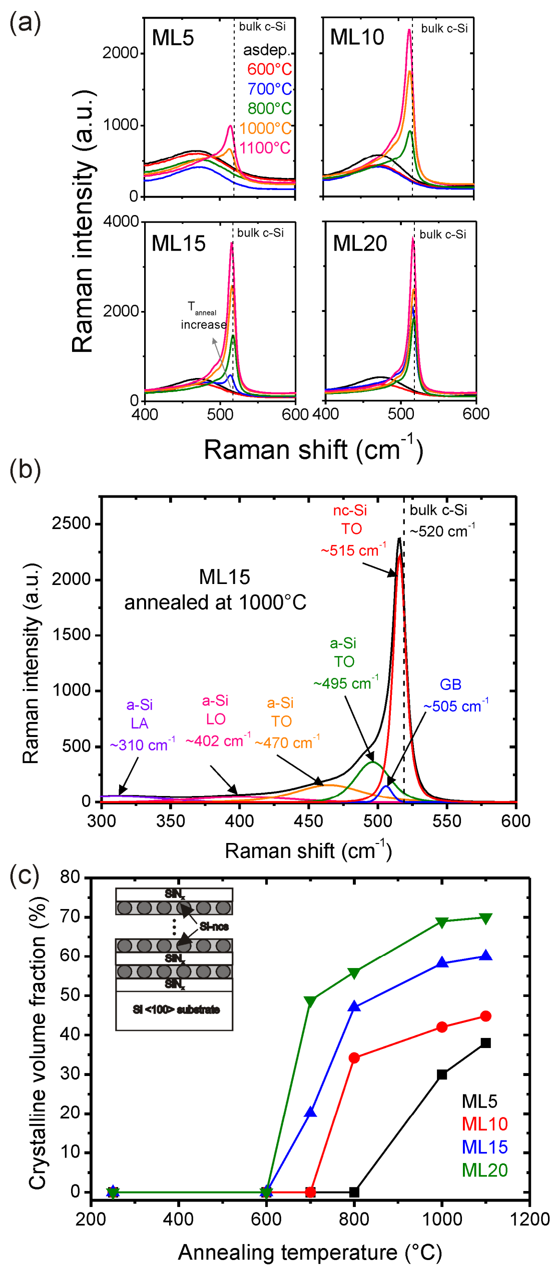

Fig. 4 (a) The first order of Raman spectra of a-Si:H/a-SiN$_x$:H multilayers before and after thermal annealing up to 1100°C in vacuum for 30 minutes prepared on quartz. (b) Deconvoluted Raman spectra of the ML15 sample annealed to 1000°C (Raman spectra of other samples were also deconvoluted, but not shown here). (c) Calculated crystalline volume fraction of samples.

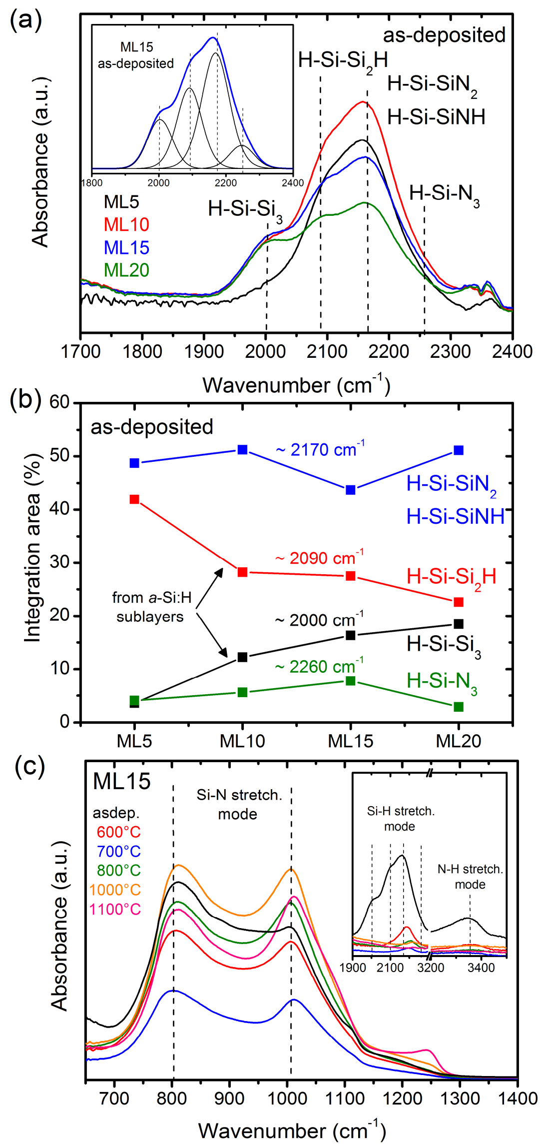

Fig. 5 (a) FTIR spectra of the as-deposited a-Si:H/a-SiN$_x$:H multilayers in region of 1700 – 2400 cm^{-1}. The inset shows a typical deconvolution of ML15 sample spectrum. (b) The comparison of the integration areas of Si-H bands. (c) The FTIR spectra of ML15 sample as-deposited and annealed up to 1100°C. The inset shows the disappearance the hydrogen from superlattice after annealing at 600°C.

ACCEPTED MANUSCRIPT

ACCEPTED MANUSCRIPT

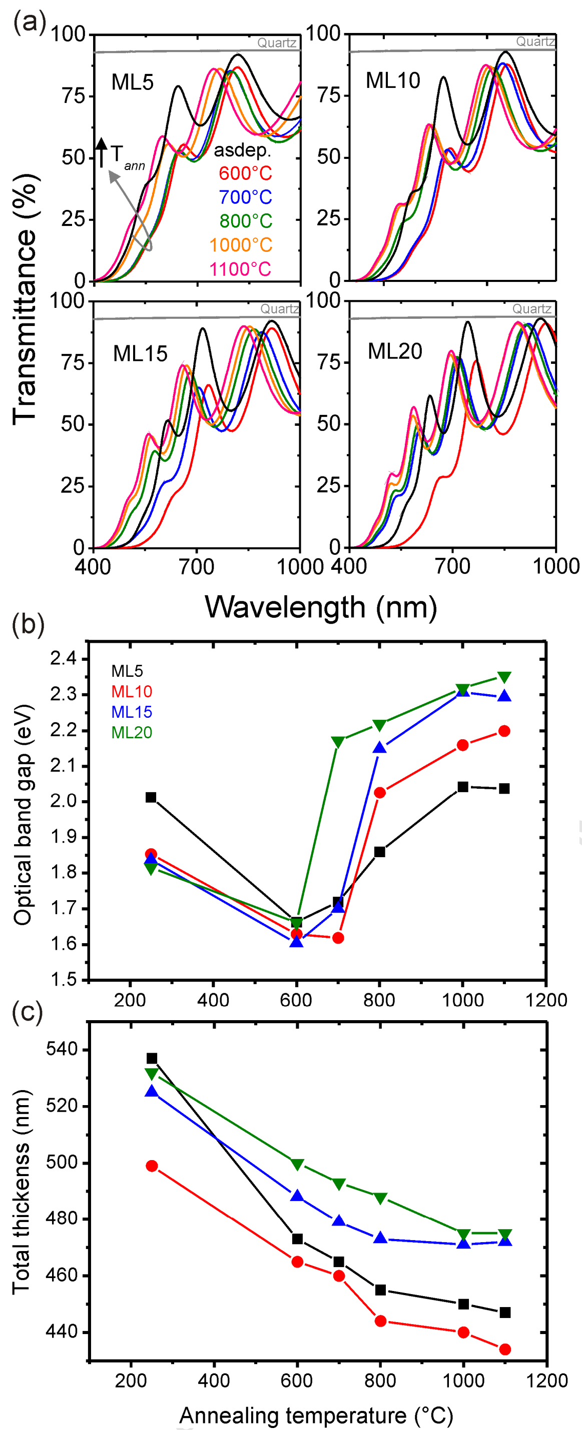

Fig. 6 (a) Transmittance of as-deposited and annealed superlattices, (b) calculated optical band gaps and (c) total thicknesses of superlattices depending on sublayer thickness and post-deposition annealing temperature.

MANUSCRIPT

Table 1 Description of a-Si/a-SiN_x:H superlattices.

Sample name	Nominal multilayer thickness (nm)		Number of sublayers	Total thickness (nm)	
	a-Si:H	*a*-SiN_x:H		Profiler	UV-Vis
ML5	5	5	121	521	537
ML10	10	10	61	490	499
ML15	15	15	41	520	525
ML20	20	20	31	534	532

ACCEPTED MANUSCRIPT

Table 2 Deposition parameters for a-Si/a-SiN$_x$:H superlattices.

Parameters	**Range**
Base pressure	<10^{-5} Pa
RF power	40 W (60mW/cm^2), 13.56 MHz
Working pressure	67 Pa
Substrate temperature	250°C
Precursor gases	SiH_4 (10% in Ar), N_2
N_2/SiH_4 flow ratio	0 and 120
Total flow rate	180 sccm
Electrode-to-substrate	20 mm
Substrates	Si(100), quartz

ACCEPTED MANUSCRIPT

ACCEPTED MANUSCRIPT

Table 3 Calculated crystallite sizes and microstrains of annealed a-Si:H/a-SiN_x:H superlattices.

Sample	***h k l***	**700 (°C)**		**800 (°C)**		**1000 (°C)**		**1100 (°C)**	
		<D> (nm)	<ε> (-)	*<D>* (nm)	<ε> (-)	*<D>* (nm)	<ε> (-)	*<D>* (nm)	<ε> (-)
ML5	*111*	a	a	a	a	3	0.040	5	0.037
	220					5	0.025	12	0.025
ML10	*111*	a	a	6	0.028	6	0.022	8	0.026
	220			6	0.011	9	0.015	8	0.014
ML15	*111*	4	0.082	4	0.039	3	0.019	5	0.022
		4	0.010	8	0.014	7	0.010	11	0.014
	220	6	0.009	9	0.008	12	0.008	9	0.006
	331	7	0.006	10	0.007	14	0.008	10	0.006
ML20	*111*	3	0.025	5	0.025	5	0.029	7	0.039
		9	0.007	9	0.007	9	0.006	17	0.010
	220	10	0.004	12	0.005	11	0.004	3	0.020
		7	0.022	4	0.017			19	0.005
	311	10	0.004	10	0.004	12	0.004	13	0.005

ACCEPTED MANUSCRIPT

ACCEPTED MANUSCRIPT

Highlights

1. NH_3-free fabrication of silicon nitride based as dielectric barrier in superlattices

2. Silicon nanostructures formed by annealing of *a*-Si:H/*a*-SiN_x:H superlattices

3. Synergy effect of analytical method in investigation of Si-NCs formation

4. Increasing in crystallization temperature with decreasing Si sublayer thickness

ACCEPTED MANUSCRIPT